Hydrogeology Journal (2015) 23: 1761–1779
DOI 10.1007/s10040-015-1298-2

Contribution of time-related environmental tracing combined with tracer tests for characterization of a groundwater conceptual model: a case study at the Séchilienne landslide, western Alps (France)

A. Vallet · C. Bertrand · J. Mudry · T. Bogaard · O. Fabbri · C. Baudement · B. Régent

Abstract Groundwater-level rise plays an important role in the activation or reactivation of deep-seated landslides and so hydromechanical studies require a good knowledge of groundwater flows. Anisotropic and heterogeneous media combined with landslide deformation make classical hydrogeological investigations difficult. Hydrogeological investigations have recently focused on indirect hydrochemistry methods. This study aims at determining the groundwater conceptual model of the Séchilienne landslide and its hosting massif in the western Alps (France). The hydrogeological investigation is streamlined by combining three approaches: a one-time multi-tracer test survey during high-flow periods, a seasonal monitoring of the water stable-isotope content and electrical conductivity, and a hydrochemical survey during low-flow periods. The complexity of the hydrogeological setting of the Séchilienne massif leads to development of an original method to estimate the elevations of the spring recharge areas, based on topographical analyses and water stable-isotope contents of springs and precipitation. This study shows that the massif supporting the Séchilienne landslide is characterized by a dual-permeability behaviour typical of fractured-rock aquifers where conductive fractures play a major role in the drainage. There is a permeability contrast between the unstable zone and the intact rock mass supporting the landslide. This contrast leads to the definition of a shallow perched aquifer in the unstable zone and a deep aquifer in the intact massif hosting the landslide. The perched aquifer in the landslide is temporary, mainly discontinuous, and its extent and connectivity fluctuate according to the seasonal recharge.

Keywords Conceptual models · Tracer tests · Hydrochemistry · Landslide · France

Received: 26 August 2014 / Accepted: 12 July 2015
Published online: 9 August 2015

A. Vallet (✉) · C. Bertrand · J. Mudry · O. Fabbri · B. Régent
UMR6249 Chrono-Environnement—Université Bourgogne Franche-Comté, 16 route de Gray, 25030, Besançon cedex, France
e-mail: aurelien.vallet@univ-fcomte.fr

T. Bogaard
Water Resources Section,
Delft University of Technology, Stevinweg 1, 2628 CN, Delft, The Netherlands

C. Baudement
CEREGE (UMR7330), Aix-Marseille University, CNRS-IRD, Europôle Méditerranéen de l'Arbois, Avenue Louis PhilibertBP 80-13545, Aix-en-Provence cedex 04, France

Introduction

Gravity is known to be the main factor in landslide motion, and water plays a prominent triggering role. Groundwater-level rise plays an important role in the (re)activation of deep-seated slope movements (Van Asch et al. 1999; Iverson 2000; Rutqvist and Stephansson 2003). Many studies have attempted to characterize the relationships between water infiltration and landslide destabilization (Alfonsi 1997; Hong et al. 2005; Helmstetter and Garambois 2010; Abellán et al. 2015; Belle et al. 2014; Bernardie et al. 2014) or to couple hydromechanical models (Cappa et al. 2004, 2006; Corominas et al. 2005; Guglielmi et al. 2005; Bonzanigo et al. 2007; Sun et al. 2009). However, to be accurate and to reflect field conditions, such approaches must be based on relevant and realistic groundwater conceptual models.

In the Alps or in the northern Apennines, most deep-seated landslides occur in crystalline bedrocks (Barla and Chiriotti 1995; Agliardi et al. 2001; Ronchetti et al. 2009). The hydrological response of a fractured-rock slope depends on the geometry and hydraulic connectivity of the discontinuity network, on individual discontinuity properties, and on the intact rock properties (Maréchal 1998; Cappa et al. 2004; Bogaard et al. 2007). In addition, vertical gradients of the hydraulic conductivity can occur with values ranging from 10^{-11} m/s at depth to 10^{-5} m/s towards the decompressed surface areas (Maréchal and Etcheverry 2003). These permeability contrasts may be sufficient to support perched aquifers (Vengeon 1998; Tullen 2002; Cappa et al. 2004; Binet 2006). Hydrogeological data strongly depend on the scale of observation (Clauser 1992), and local measurements are

rarely representative of the overall behaviour of the aquifers. Heterogeneous, anisotropic and discontinuous properties of fractured rocks are accentuated by the landslide deformation and by the presence of weathering products (colluvium, clay) filling the open fractures (Cappa et al. 2004; Binet 2006).

Although piezometers can give significant, yet local, insights on the groundwater system (Kosugi et al. 2011; Padilla et al. 2014), their cost, their short lifespans in unstable areas and their poor representativeness make piezometers seldom used in landslide studies (Michoud et al. 2013). Consequently, recent studies focus on indirect methods such as hydrochemistry surveys by monitoring springs for natural and artificial tracers (Bogaard et al. 2007). For example, recent studies have demonstrated that the recharge area of a landslide can be larger than the landslide itself (Guglielmi et al. 2002) or that the landslide groundwater variations can be significantly controlled by deep groundwater flows (Ronchetti et al. 2009). In addition, hydrochemical methods can discriminate waters which flowed through the stable rock masses from those which flowed through the unstable rock masses (Binet et al. 2009). Methods are mainly based on chemical analyses of major elements (Cappa et al. 2004; Binet et al. 2007a), but additional parameters can be used to identify and quantify specific processes. These parameters include water stable isotopes (Guglielmi et al. 2002; Lin and Tsai 2012), trace elements (Cervi et al. 2012), natural fluorescence (Charlier et al. 2010) and artificial tracers (Bonnard 1988; Binet et al. 2007b). However, hydrochemistry surveys are time-consuming, expensive and require specific expertise. Consequently, many landslide studies are based on a few field visits and do not provide anything more but a snapshot of the hydrogeological conditions (Vengeon 1998; Guglielmi et al. 2002; Binet et al. 2007a).

This contribution aims at characterizing the groundwater conceptual model of the Séchilienne landslide and its hosting massif. This case study aims at streamlining the hydrogeological investigation methods by combining three complementary approaches: (1) a one-time multi-tracer test survey during a high-flow period, (2) a seasonal monitoring of the water stable isotope content and the water electrical conductivity, and (3) a hydrochemical survey during low-flow periods. These three complementary approaches allow for determination of: (1) flowpaths and residence times of the groundwater, (2) average recharge elevations and hydrodynamic behaviour of springs at season time-steps, and (3) spring chemical clusters and water origin.

Materials and methods

Investigation strategy background

It is crucial to characterize the groundwater-flow pattern during high-flow periods since it is during these periods that the landslide destabilisation triggered by large amounts of recharge is the strongest. Moreover, under high-groundwater-level conditions, flowpaths not existing in the drier seasons can occur as well as higher flow rates, thus allowing increase in the probability of tracer restitution at springs. Fluorescent tracers are used in this study as they show a high sensitivity analysis, low detection limits, and low toxicity levels (Leibundgut et al. 2011). Tracer test settings can be used to characterize (1) the extension of the recharge area of the unstable slope, (2) groundwater flowpath hypotheses by investigating the contribution of a spatially constrained area, (3) the presence or not of a perched drainage in the disturbed zone, (4) the role of the main fractures involved in the groundwater flow and (5) groundwater flow velocities. The recovery rate of the tracer can further help quantify the hydraulic properties of the aquifer (Cappa et al. 2004; Binet et al. 2007b).

The dual-permeability of fractured reservoirs involves complex hydraulic connections between rare strongly conductive fractures and numerous poorly conductive fractures (Cappa et al. 2004). The poorly conductive fractures are hereafter referred to as micro-fissured matrix. The seasonal fluctuation of the chemistry of a spring can inform on the proportion of the spring that is recharged through the conductive fractures (reactive medium) and/or the micro-fissured matrix (inertia of the aquifer promoting water–rock interaction; Pili et al. 2004). Springs supplied by conductive fractures are thus expected to show high seasonal variations in water chemistry compared to springs supplied by the micro-fissured matrix. In addition, the fluctuation of the saturated-zone depth, controlled by the seasonal recharge variability, can modify the hydraulic connections and the groundwater flowpaths of the fractured reservoir. Springs supplied by a well-developed and well-connected network of conductive fractures will show a significant seasonal variation related to the elevation of their average recharge area, whereas the springs supplied by the micro-fissured matrix will show less seasonal variation. Lastly, the recharge areas of springs supplied through extended networks of conductive fractures will be significantly larger than the recharge areas of springs only supplied by the micro-fissured matrix. For all these reasons, the analysis of seasonal variations of chemistry and of recharge-area elevation of springs (seasonal pattern, dispersion, amplitude …) can be used to qualitatively characterize the hydrodynamic behaviour of the aquifer.

During low-flow periods, the groundwater flow is mainly driven by the aquifer drainage, with low external disturbance (low recharge). As a consequence, the chemical content of the groundwater is controlled by the mineral dissolution rates and the water–rock interaction duration, and is independent from the recharge influence (Hilley et al. 2010). The hydrochemical analysis enables one to distinguish various water chemical groups and to compare them with the massif lithology. This comparison provides information about water origin, residence time and flowpaths. The groundwater chemistry can also be influenced by the landslide hydromechanical processes, thus distinguishing water which flowed through the unstable zone from the water which did not flow through

 DOI 10.1007/s10040-015-1298-2

the unstable zone (Binet et al. 2009). In addition, geochemical inverse modelling allows one to characterize solid phases involved in the water–rock interaction processes, to estimate the mass transfers and to validate the flowpath hypotheses with the results of tracer tests and $\delta^{18}O$ values (Cervi et al. 2012).

Study site

Study area

The Séchilienne landslide is located to the south-east of Grenoble (France), on the right (north) bank of the Romanche River, on the southern slope of the Mont-Sec massif (Fig. 1a). The landslide is located in the Belledonne crystalline range and is composed of micaschists. The micaschists are characterized by a N–S-trending vertical foliation. Carboniferous to Liassic sedimentary deposits unconformably cover the micaschists along the massif ridgeline, above the unstable zone. Locally, glacio-fluvial deposits overlie both the micaschists and the sedimentary deposits. Micaschists mainly consist of quartz, biotite, phengite and chlorite, with occurrences of quartz-albite granoblasts, carbonate veins, and disseminated pyrite (Vengeon 1998). Liassic deposits consist of limestones with intercalation of breccia-rich layers containing fragments of coal, micaschists and dolomites, while Triassic deposits are represented by sandstone, quartzite, dolomite and minor intercalation of black shales and argillites. Carboniferous deposits are characterized by micaceous black shales, sandstones and conglomerates with intercalations of anthracite (Barféty et al. 1972; Vengeon 1998). Fluvio-glacial and colluvial deposits contain reworked materials from the previously cited formations.

Séchilienne unstable slope

The Séchilienne landslide is limited eastwards by a N–S fault scarp and northwards by a major head scarp of several hundred meters wide and tens of meters high below the Mont Sec. Rare geomorphological evidence allows for precise definition of the western and southern boundaries of the unstable area. The Séchilienne landslide is characterized by a deep progressive deformation controlled by the network of faults and fractures. A particularity of the Séchilienne landslide is the absence of a well-defined basal sliding surface. The landslide is affected by a deeply rooted (about 100–150 m) toppling movement of the N50–70° slabs to the valley (accumulation zone) coupled with the sagging of the upper slope (depletion zone) beneath the Mont Sec (Vengeon 1998; Durville et al. 2009; Lebrouc et al. 2013). Lastly, a very actively moving zone, where high displacement velocities are measured (from 150 to 300 cm/year on average), is distinguishable from the unstable slope (from 2 to 15 cm/year on average). The Séchilienne landslide is characterized by a good correlation between antecedent cumulative precipitation and average displacement velocities (Rochet et al. 1994; Alfonsi 1997; Durville et al. 2009; Chanut et al. 2013). Helmstetter and Garambois (2010) showed a weak but significant correlation between rainfall signals and rockfall micro-seismicity. Vallet et al. (2015) showed that the Séchilienne displacement rates are better correlated to the recharge than to the precipitation, reinforcing the significant role of groundwater flow in the Séchilienne destabilization. Because of the mountainous location of the studied landslide, precipitation consists of rain and snow. Annual snow amount is 7-fold lower than rainfall. Unlike the groundwater recharge which shows high seasonal contrasts (dry summers vs. wet winters), precipitation does not show any pronounced seasonal tendencies. Since groundwater controls the Séchilienne destabilisation, the landslide velocity also shows seasonal contrasts (low velocities in summer vs. high velocities in winter, Fig. 1b).

Hydrogeological background

The landslide is highly fractured and shows a much higher hydraulic conductivity than the intact underlying bedrock (Vengeon 1998; Meric et al. 2005; Le Roux et al. 2011), thus leading to a perched aquifer in the landslide (Guglielmi et al. 2002). Besides this, a deep saturated zone at the base of the slope is hosted by the fractured metamorphic bedrock over the whole massif bearing the landslide, with a thick (about 100 m) vadose zone above it. Although the Séchilienne landslide has already been investigated by two distinct hydrochemistry snapshot surveys (Vengeon 1998; Guglielmi et al. 2002), groundwater flow mechanisms responsible for recharge of the perched aquifer in the landslide (hereafter referred to as landslide perched-aquifer) are still debated.

Vengeon (1998) showed that the landslide perched-aquifer is recharged by water-level rises of the deep saturated zone, whereas Guglielmi et al. (2002) showed that the main recharge originates from a perched aquifer in the sedimentary cover (hereafter referred to as sedimentary perched-aquifer). Conclusions are mainly based on rough water-balance estimation, geological observations and limited hydrogeology data. Indeed, the Séchilienne site presents a spatially sparse hydrogeological network. First, no springs are located in the unstable zone. Second, surrounding springs are scattered in the massif and are subject to a strong anthropic pressure (water diversion) which makes spring flow measurements impossible and hinders the analyses.

Monitoring sites

Hydrochemistry data and the conceptual models of Vengeon (1998) and Guglielmi et al. (2002) were used as a baseline to design the monitoring network (Fig. 1a) and to select the injection locations of the artificial tracers. Table 1 details the location name and the type of each monitoring network point. Most of the monitored spring flows (Fig. 1a) are (1) the overflow leftover from water withdrawals (S5, S6, S9, S11, S13, S15, S18, S19, S20, S21, S25), (2) single points in areas with multiple

DOI 10.1007/s10040-015-1298-2

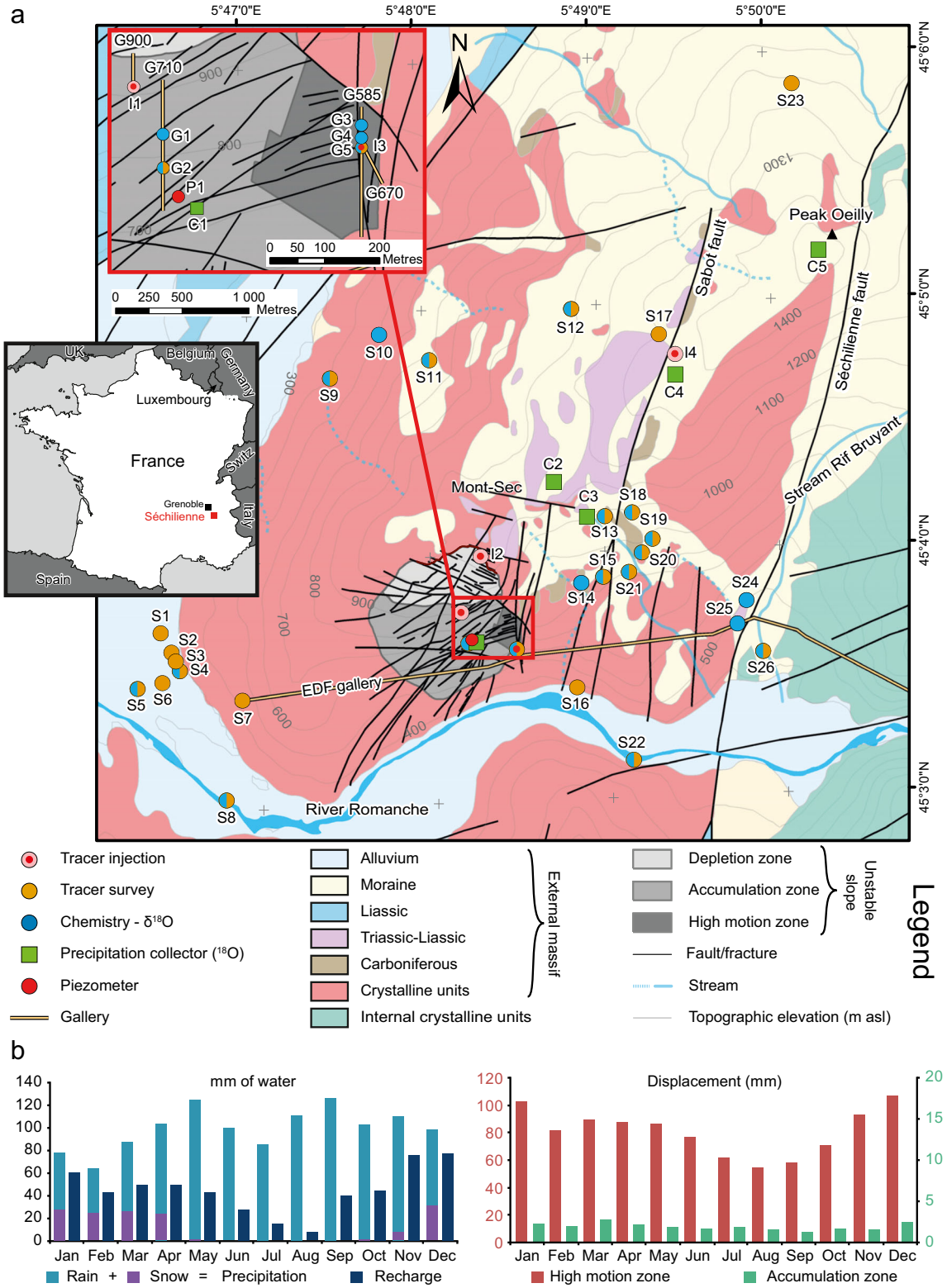

Fig. 1 Séchilienne site. **a** Landslide site map and monitoring network. **b** Climatic and landslide kinematic settings based on the monthly-cumulated amounts of rainfall, snowfall, recharge and displacements averaged over the years from 1993 to 2013. The unstable slope boundary is defined according to the geophysical survey of Le Roux et al. (2011). Recharge was computed according to the computation workflow of Vallet et al. (2015) based on temperature and precipitation records of the Mont-Sec meteorological station

resurgences, (S1, S2, S3, S4, S10, S12, S14, S24, G5) and (3) water collected by vinyl sheets in galleries, which constitutes the mean water leakage/inflow from those galleries (G1, G2, G3, G4).

 DOI 10.1007/s10040-015-1298-2

Table 1 List of monitoring network locations and type

Location code	Location name	Type
S1	Vizille	S
S2	Vizille	S
S3	Vizille	S
S4	Vizille	S
S5	Dhuy	S
S6	Reine	S
S7	Gallery EDF	G
S8	Romanche	R
S9	Cornier	S
S10	Chemin Mont-Jean	S
S11	Mont-Jean	S
S12	Pleney	S
S13	Fonafrey	S
S14	Thiebaud-EDF	S
S15	Thiebaud-Lavoir	S
S16	Noyer-Chute	S
S17	Clobasse	S
S18	Clos-Bénit	S
S19	Finet	S
S20	Les Mathieux	S
S21	La Bathie	S
S22	Romanche	R
S23	Mulet	S
S24	Les Aillouds	S
S25	Mounier	S
S26	Rif-Bruyant	R
C1	Gallery 710	Rc /L
C2	Madeleine	Rc / L
C3	Fonafrey	Rc
C4	Rochassier	Rc
C5	Pic-Oeilly	Rc
G1	Gallery 710-1	G
G2	Gallery 710-2	G
G3	Gallery 585-1	G
G4	Gallery 585-2	G
G5	Gallery 585-3	G
I1	Gallery 900	IS
I2	Crevasse	IS
I3	Gallery 585	IS
I4	Rochassier	IS
P1	Gallery 710	P

G gallery outlet or water inflow, *IS* infiltration structures such as crevasse/fractures/sinkholes, *L* lysimeter, *S* spring, *R* river, *Rc* rain collector, *P* piezometer

Among the 30 springs identified in the Séchilienne massif, none are located in the unstable zone. However, three former mining galleries, situated at 900, 670 and 585 m asl (G900, G670, G585), and a gallery excavated to survey the landslide at 710 m asl (G710), are located within the unstable zone, with lengths of 60, 88, 240 and 240 m, respectively (Fig. 1a). These galleries have a north–south orientation, except G670 which is oriented N155 and which intersects the unstable zone. Galleries G585 and G710, both located in the unstable zone, show water inflow and/or leakage suitable for monitoring. Unfortunately, G585 is no longer accessible and was only sampled by Vengeon (1998), and monitored as part of tracer test surveys. Another gallery (EDF gallery, French Electricity Company) is also located at the foot of the landslide slope at an elevation of about 425 m asl. Except for the EDF gallery where some highly fractured zones are covered with concrete, these galleries show bare rock.

A piezometer (P1) is located near the G710 gallery, which was active from November 2009 to April 2010, before being clogged. For the water isotope survey, five hermetically closed rain collector tanks (C1, C2, C3, C4 and C5) were buried about 1 m deep and wrapped with an isotherm cover to avoid isotope fractionation due to the fluctuations of the atmosphere temperature. Rain collector points were installed every 200 m at elevations from 640 to 1,520 m asl, covering most of the massif hosting the landslide (Fig. 1a). Two rain collectors (C1 and C2) were installed in woodland and in grassland (the two main vegetation types of the landslide recharge area), respectively, and were each coupled with a lysimeter.

The EDF gallery outlet (S7), the Romanche River (S8 and S22) and the Rif Bruyant stream (S26) were occasionally added to the monitoring program. Additionally, the EDF gallery was also monitored for a unique water chemistry survey (March 2002) during maintenance of the EDF gallery. The G900 gallery was used only for tracer test surveys. Demolition works of a hydropower plant, after the tracing survey, modified the flowpath of S16 spring, which is now flowing directly to the alluvial aquifer. S23 and S17 were only monitored with tracer test surveys.

Methodology

Tracer test surveys were performed in two campaigns, in April 2001 and in March 2002. The March 2002 survey was coupled with a hydrochemical survey of the water inflows in the EDF gallery. Hydrochemical surveys were conducted from September 2010 to September 2012. To take account of seasonal variations, the surveys included: (1) four isotopic campaigns (26 spots), performed quarterly, coupled with 12 water electrical conductivity (EC) surveys, and (2) five hydrochemistry surveys (21 spots) performed in low-flow periods, from early June to late September. The four isotopic campaigns were performed at 3-month intervals: December 2011, March 2012, June 2012 and September 2012. Hydrochemical data of the G585 gallery (Vengeon 1998), were also integrated into this study. Lastly, water inflows observed in the five galleries (Vengeon 1998) were analysed in order to identify saturated and unsaturated zones inside the landslide body and to infer the depth to the water level within the unstable slope.

Tracer tests

A four-tracer test survey was implemented in April 2001 in the Séchilienne unstable slope recharge area. Different fluorescent tracers were injected at four carefully chosen locations (Fig. 1a; Table 2).A sinkhole (I4) located along the Sabot fault (Fig. 1a) was selected as a representative infiltration location of the top sedimentary cover to evaluate the extent of the recharge area. A crack located in the depletion zone (I2) was chosen to represent the infiltration on the summital landslide area. A depression zone (I1) located in the accumulation zone near the mine

DOI 10.1007/s10040-015-1298-2

Table 2 Settings of the multi-tracer test of April 2001 and single tracer test of March 2002

Injection location	Tracer	Date	Tracer amount (kg)	Injected water volume (m^3)
I2	Rhodamine	10-April-2001 10:00	5	8
I1	Sodium naphtionate	10-April-2001 13:00	6	30
I4	Uranin	10-April-2001 17:00	8	3
I3-A	Eosin	11-April-2001 12:00	5	N/A
I3-B	Uranin	13-March-2002 8:30	5	N/A

gallery G900 was chosen to test the hydraulic conductivity of the N70 near-vertical fractures. A sink in the mine gallery G585 (I3) was chosen as an injection spot to test the infiltration on the N–S fault zone bordering the rapidly moving landslide zone. Since the EDF gallery was flooded at the time of the survey, detailed monitoring of the water inflow points was not possible. A second tracer test was performed in March 2002 when the gallery was emptied for maintenance. Due to the impossibility of measuring the flow rate of springs, the tracer velocities were obtained by dividing the distance (in a straight line) between injection and spring points by the shortest tracer transit times.

Special instruments and sample rates were implemented for the two tracer tests (in 2001 and 2002). For the multi-tracing survey performed in April 2001, monitoring lasted for 2 months, and a sample rate was adapted according to survey time by decreasing the sampling resolution. G5, S5 and S6 springs were monitored with an automatic sampler, while activated charcoal packets were implemented and manual water samples were taken at S1, S4, S9, S11, S13, S15, S18, S19 and S20. Only charcoal monitoring was performed on the remaining springs. For the reiterated tracer test from gallery G585 (I3-B test), only hand sampling was performed in all water inflows of the EDF gallery, between kilometric points 5 and 7 during the 2 days following the injection day (Fig. 3).

Seasonal analysis and spring mean recharge-area elevation

In order to distinguish the main springs flowing through conductive fractures from those flowing through the micro-fissured matrix, analyses of the seasonal variations of chemistry and of recharge-area elevation were undertaken. These analyses are based on the water electrical conductivity (EC) and on the water stable isotope ratio ($\delta^{18}O$). EC is representative of the water total mineralization; $\delta^{18}O$ allows for the estimation of the recharge-area elevation of a spring (see next section).

For each spring, the seasonal variations of EC and recharge-area elevations were investigated based on (1) the seasonal scattering (based on the standard deviation (SD) of the samples of the seasonal campaigns) and on (2) the seasonal patterns. In addition, the average elevation of the recharge area for each spring was estimated from the elevation values deduced from the four water sampling campaigns. The difference between the average elevation of the recharge area and the elevation of the spring-associated ridgeline point (see next section), expressed in percent, will distinguish springs having local recharge areas from those having remote recharge areas.

A spring is considered to be mainly supplied by the conductive fractures if the seasonal variations of EC and elevation of the recharge area show a high scattering and clear seasonal pattern (that is, high EC values in summer and low EC values in winter, and low elevation values in summer and high elevation values in winter). This interpretation can be reinforced if a geological structure (e.g., fault) links up the average elevation of the recharge area and the spring location. In this case, a remote recharge area is expected. Conversely, a spring is considered to be mainly supplied by the micro-fissured matrix if the seasonal variations of EC and elevation of the recharge area show low scatterings and unclear seasonal pattern. This interpretation can be reinforced if no geological structure links up the average elevation of the recharge area and the spring location. In this case, a local recharge area is expected. Intermediary spring behaviour can be identified between these two groups and others factors can influence the spring signal (surface network, local perched aquifer, etc.).

Estimation of the mean elevation of the spring recharge area from $\delta^{18}O$ measurements

Water stable isotope fractionation is thermo-dependent, leading to a series of effects on the isotope fractionation (Clark and Fritz 1997). At the scale of a landslide site, only the elevation effect and seasonal effects have a non-negligible impact on the isotope fractionation (Leibundgut et al. 2011). The determination of the local elevation gradient (elevation=$a\times\delta^{18}O+b$) enables the determination of the average recharge elevation of the sampled springs. Generally, the seasonal effect, which can significantly influence the elevation effect, makes it necessary to characterize the local elevation effect for each sampling campaign, as was done in this study.

In mountainous areas, a local calibration of the isotopic gradient is generally possible, using springs with well-defined recharge areas. In the case of the Séchilienne landslide, no such springs allow for estimation of the isotope elevation gradient. Instead, five rainfall collectors were settled to characterize the $\delta^{18}O$ signal (Fig. 1a). The infiltration isotopic signals can be modified from the precipitation initial signal through the soil layers by evaporation processes, leading to $\delta^{18}O$ enrichment (Gat 1996). Two rainfall collectors were therefore coupled with a lysimeter in order to evaluate the evaporation impact on the actual $\delta^{18}O$ infiltration signal.

 DOI 10.1007/s10040-015-1298-2

Because the hydrodynamic properties of the aquifers can delay or buffer the infiltration signal, the spring water does not generally correspond to the last rainfall period; therefore, instantaneous synchronization of $\delta^{18}O$ water sampling for both springs and rainfall collectors would not be relevant. To take into account the transit through the aquifer, the spring water $\delta^{18}O$ signal was compared with the $\delta^{18}O$ signal of a cumulated amount of precipitation that fell during the period between two consecutive spring sampling campaigns (about 3 months); thus, the isotopic signal of the rain collectors corresponds to the precipitation $\delta^{18}O$ signal weighted by the 3-month rainfall amount. The 3-month period is based on the study of Vallet et al. (2015) which shows that the best R^2 coefficient of determination between the cumulative groundwater recharge and the landslide velocity is obtained for periods from 68 to 132 days. As the landslide velocity is mainly controlled by the pore-water pressure, these periods can be considered as representative groundwater residence times. The isotope elevation gradient of precipitation is determined with the $\delta^{18}O$ data of the five rain collectors. The isotope elevation gradient of infiltration is considered identical to the slope of the isotope elevation gradient of precipitation and only the intercept is adjusted to fit to the lysimeter $\delta^{18}O$ measurements, assuming that evaporation is homogeneous (Fig. 2a). The elevation of the spring recharge area is estimated from the *infiltration* isotope gradients for the April–June and July–September sampling campaigns, for which actual evaporation is significant, and from the *precipitation* isotope gradient for the October–December and January–March sampling campaigns.

In order to locate the recharge area of the springs, the steepest slope line is drawn for each spring, up to the ridgeline, based on a digital elevation model with a 25-m resolution (Fig. 2b), which allows for the definition of a ridgeline point associated to each spring. If the $\delta^{18}O$-derived elevation of a spring recharge area falls between the spring elevation and the spring-associated ridgeline point elevation (materialized by the steepest slope straight line, Fig. 2b), then the recharge area will be considered as local. In this case, the groundwater flow is thought to follow the topographic gradient without any influence or disturbance linked to geological features such as fractures or faults (hereafter referred to as topographic control). Otherwise, the $\delta^{18}O$-derived elevation of the spring recharge area will be placed along the ridgeline, at the nearest corresponding elevation, and the recharge area of the spring will be considered as remote. In this case, the groundwater flow is thought to be controlled by geological features (hereafter referred to as structural control).

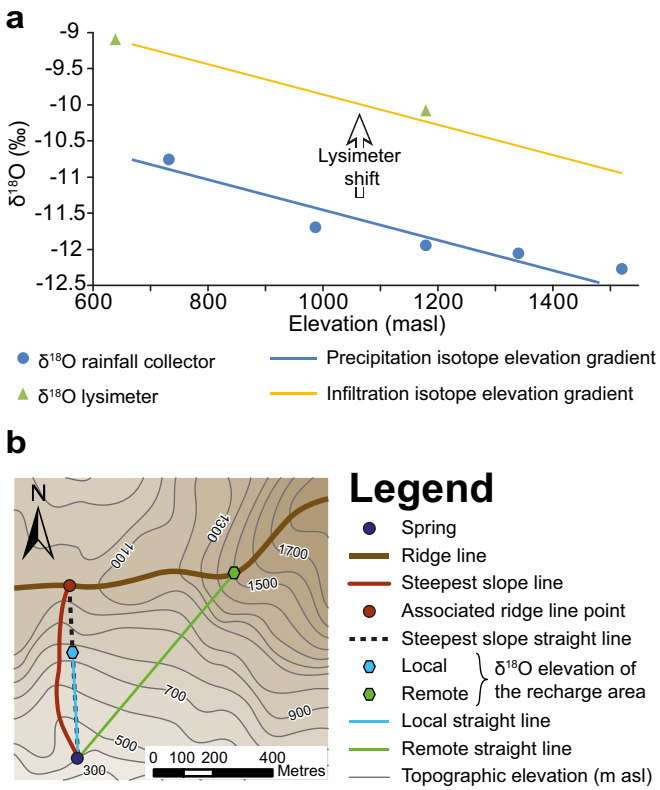

Fig. 2 Illustration of the methods implemented for the $\delta^{18}O$ analysis. **a** Determination of the isotope elevation gradient for precipitation and infiltration. **b** Spatial representation (map) of the $\delta^{18}O$ elevation of the spring recharge area

Hydrochemical analysis

The chemical analysis of samples from low-flow periods enables distinction between water end-members flowing from sedimentary, unstable and/or stable fractured reservoirs, and the mix between these end-member reservoirs. Groundwater chemistry is discussed using major ion concentrations. The nature and origin of the various springs is established by using a Durov diagram, which allows for characterization of the relationships between the chemical type (function of encountered rock types) and the electrical conductivity (degree of mineralization). Hydrochemistry is complex as the alteration of each of the three distinct rocks (moraines, carbonates and micaschists) produces the same ions (Table 3).

Major ion combinations are used to characterize the water origin and the flowpaths: Ca vs. HCO_3 for the sedimentary cover and Na vs. Cl to distinguish a precipitation origin from alteration of the micaschist

Table 3 Origin of minerals according to rock types from Vengeon (1998) and structural formulae established from the LLNL database (Parkhurst and Appelo 1999)

Lithology	Mineral	Structural formula	Water ion release
B	Albite	$NaAlSi_3O_8$	Na, HCO_3
B	Muscovite	$KAl_3Si_3O_{10}(OH)_2$	K, HCO_3
B	Clinochlore-14A	$Mg_5Al_2Si_3O_{10}(OH)_8$	Mg
B	Phlogopite	$KAlMg_3Si_3O_{10}(OH)_2$	Mg, K
B (veins)/SC	Calcite	$CaCO_3$	Ca, HCO_3
SC	Dolomite	$CaMg(CO_3)_2$	Ca, Mg, HCO_3
B	Goethite	FeOOH	Fe
B	Pyrite	FeS_2	Fe, SO_4, H

B bedrock; *SC* sedimentary cover

DOI 10.1007/s10040-015-1298-2

(albite). In addition, the water content variations for each identified hydrochemical facies are investigated with Stiff diagrams. The hydrochemical facies deduced from the previous analyses are then spatially compared with the distribution of the geological formations. A geochemical inverse model is performed on the spring chemical contents and rock mineral phases, using PHREEQC 3.1.1 code (Parkhurst and Appelo 1999) and the LLNL database (Lawrence Livermore National Laboratory thermodynamic database, *llnl.dat*). In this study, inverse modelling is used first to identify mineral phases and mass transfers involved in the water–rock interaction processes and, second, to validate flowpath hypotheses deduced from tracer tests and $\delta^{18}O$ analyses.

The inverse model is tested for springs representative of both the stable and unstable zones. The initial water chemistry of the inverse model (Table 4) matches with the average composition of Alpine rainwater (Atteia 1994). Minerals representative of the sedimentary cover and micaschist bedrock (Table 4) were chosen based on the work of Vengeon (1998); also taken into consideration were gaseous phases (O_2 and CO_2) in the inverse model.

Sample analysis

Survey of the tracer tests

Artificial tracers (Uranin, Eosin, Rhodamin B and Sodium naphtionate) were extracted from charcoal adsorbents using an eluent (ethanol mixed with ammonia) by a fluorescence spectrometer (Perkin-Elmer LS 30 UV-spectrometer). Accuracy depends on the natural organic matter content, which is highly variable through precipitation events. Analyses by fluorescence spectrometry were performed at the Chrono-Environnement laboratory at the University of Franche-Comté, France.

Oxygen stable isotope

Water samples were collected in glass vials with caps with an additional parafilm to prevent any possible evaporation. The oxygen stable isotope was analyzed with a liquid water isotope analyzer method (LWIA) using an off-axis integrated cavity output spectroscope (OA-ICOS), model DLT-100, manufactured by Los Gatos Research Inc. For more details about method accuracy, precision and repeatability, see Penna et al. (2010) and Lis et al. (2008). Isotopic analyses were performed at the Faculty of Civil Engineering and Geosciences at the Delft University of Technology in the Netherlands.

Table 4 Initial water rainwater composition from Atteia (1994) used in the inverse model. a_{H^+} and a_{e^-} are respectively hydrogen and electron activities

Parameter	Value
Temp (°C)	20
pH=−log a_{H^+}	6
pe=−log a_{e^-}	4
Ca (meq/L)	$3.85E^{-02}$
Mg (meq/L)	$4.42E^{-02}$
Na (meq/L)	$7.39E^{-03}$
K (meq/L)	$1.25E^{-03}$
Fe (meq/L)	$5.45E^{-05}$
Al (meq/L)	$1.15E^{-04}$
SO_4 (meq/L)	$1.50E^{-02}$
Cl (meq/L)	Equilibrate
HCO_3 (meq/L)	$2.41E^{-02}$
SiO_2 (mmol/L)	$5.30E^{-01}$

Field measurement

The pH, water electrical conductivity and temperature were measured on site with a WTW apparatus, model LF30 (a Xylem Inc. branch). The probes were calibrated before each campaign with standard buffer solutions. Measurements are reduced to the standard temperature of 25 °C with a respective accuracy of 0.1 pH units and 0.1 μS/cm.

Water chemistry analysis

Water samples were collected in polyethylene bottles and were filtered at 0.45 μm. Analyses of Na^+, Ca^{2+}, K^+, Mg^{2+} were performed by atomic absorption spectrometry (AA 100 Perkin–Elmer) with detection limits of 0.01, 0.5, 0.1 and 0.1 mg/L, respectively. Analyses of SO_4^{2-}, NO^{3-} and Cl^- were performed by high-pressure ion chromatography (Dionex DX 100) with detection limits of 0.1, 0.05 and 0.1 mg/L, respectively. The concentrations in HCO_3^- were measured by acid titration with N/50 H_2SO_4, within at most 48 h after sampling, with 1 % accuracy. For the Séchilienne hydrochemical conditions (pH between 6 and 8.5), total and carbonate alkalinity can be considered as equalling HCO_3^- concentration. Only analyses which have a charge balance lower than 10 % were taken into account. Silica was analyzed with a spectrophotometer (Spectroquant, Pharo 300, Merck) using a silica-test kit (Merck) with 3 % accuracy. Chemistry analyses were performed at the Chrono-Environnement Laboratory at the University of Franche-Comté.

Results and discussion

High-flow periods: tracer test survey

For the I4 test (Fig. 3a), the G1 water inflow displays the highest tracer velocity (3 km/day). Numerous springs (S13, S16, S20 and S21) located along the N20 Sabot fault are positive for tracer detection, with velocities ranging from 0.45 to 0.84 km/day. The same is observed for the outlet S7 of the EDF gallery (0.88 km/day). The velocity contrast between G1 and the other positive springs indicates that the drainage by the unstable slope bypasses the N20 faults and is supported by near-surface drainage between the sedimentary cover and the unstable slope perched aquifers. This test also demonstrates the prominent role of the Sabot fault and the EDF gallery in the drainage of the slope.

DOI 10.1007/s10040-015-1298-2

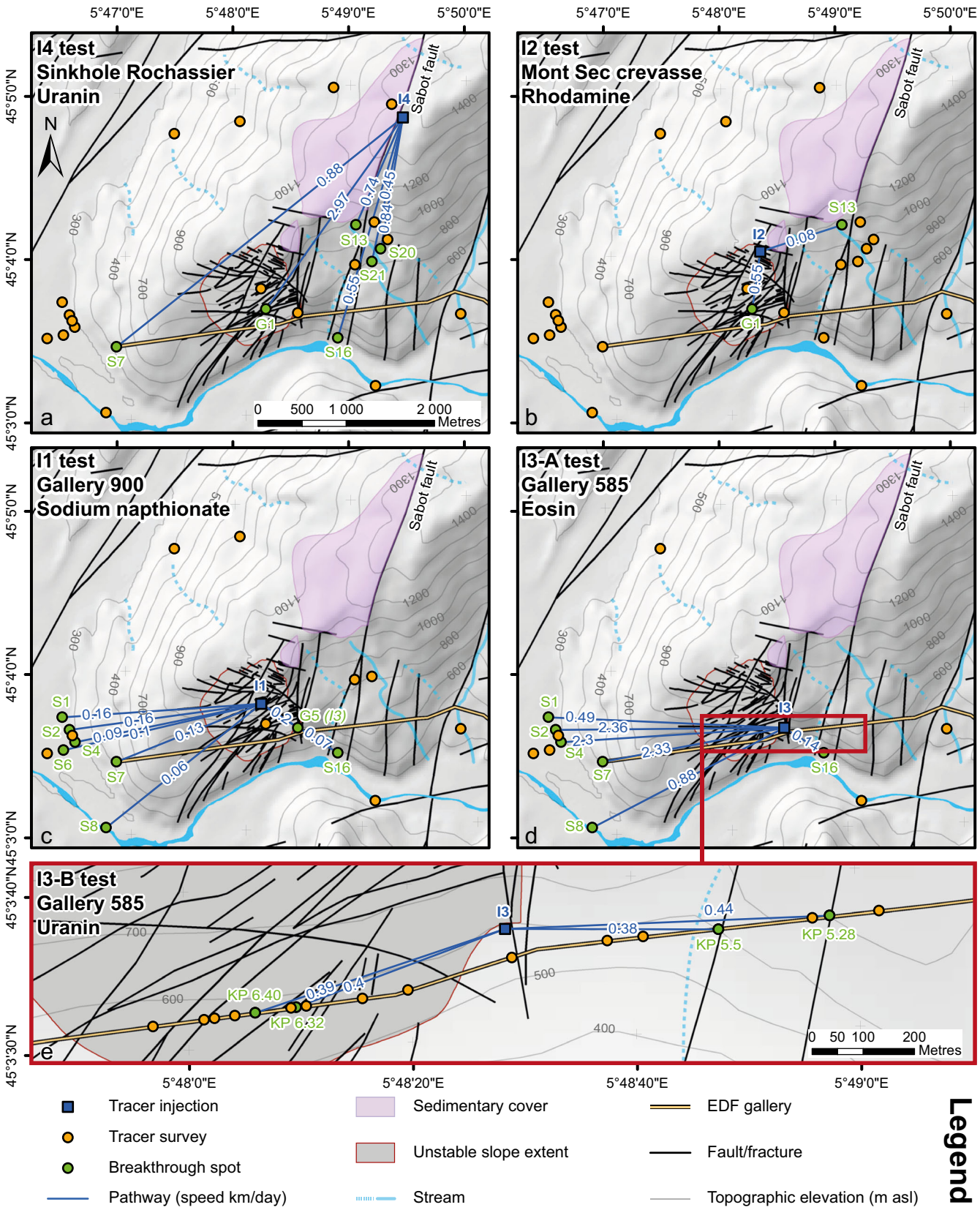

Fig. 3 Tracer-test analysis of April 2001 and March 2002 campaigns with **a** I4 test, **b** I2 test, **c** I1 test, **d** I3-A test and **e** I3-B test

For the I2 test, only G1 and S13 are positive (Fig. 3b). A large velocity difference can be observed between the down-slope flows, 7-fold faster than the lateral flow towards the N20 fault (0.55 vs. 0.08 km/day). This

DOI 10.1007/s10040-015-1298-2

difference can be attributed to the dense opened-fractures network and to the highest hydraulic gradient along the steepest slope. This test demonstrates the significant drainage role of the unstable slope and also the role of the N20 Sabot fault.

The I1 test highlights a main westward drainage component, except for S16 and G5 springs (Fig. 3c). In this part of the unstable zone, the groundwater flow is very likely supported by the dense network of N70 fractures and by the EDF gallery. In contrast, the southeast drainage seems to be supported by the Sabot fault. The average velocities range between 0.06 and 0.16 km/day. The first test in gallery G585 (I3-A test, Fig. 3d) is detected at the EDF gallery outlet (S7), confirming the drainage role of the EDF gallery. High velocities (0.49 to 2.36 km/day) are observed for the western springs, contrary to the eastern S16 spring (0.14 km/day).

The second G585 test (I3-B test, Fig. 3e) is positive at four kilometric points (KP): 5.28 and 5.50 to the east, demonstrating the influence of the N20 Sabot fault, and 6.32 and 6.40 to the west, confirming the role of the EDF gallery in the collection of a part of the water flowing from the N70 fractures.

A comparative analysis of the four tracer tests improves the characterization of groundwater flow in the massif. S7 showed high velocity (2.33 km/day) during the I3-A test (Fig. 3d) and the EDF gallery water inflows show low velocities (about 0.4 km/day) during the I3-B test. For both tests, first tracer arrival times are similar (about 1 day). The velocity contrast between the two tests can be explained by the quasi-instantaneous transit along the EDF gallery, which leads to overestimating groundwater velocities to the EDF gallery outlet S7. The S7 tracer velocity for the I3-A test can be estimated independently of the gallery transit at 0.4 km/day instead of 2.33 km/day. This estimated velocity is similar to the EDF gallery tracer velocities observed during the I3-B test. The I1 and I3 tracer tests indicate the same velocity magnitudes for S7 and for some of the western springs (S2 and S4), suggesting that these western springs are partly recharged by water from the EDF gallery. The EDF acts as a by-pass of the groundwater flow. The high speeds of the western springs (S2 and S4) during the I3-A test, similar to the S7 outflow, show that these springs are likely influenced by the EDF gallery outflow.

The I2 test shows a high velocity toward G1 (0.55 km/day) as does the I1 test toward G5 (0.2 km/day). These high velocities reveal a high transmissivity of the unstable zone promoted by a dense fracture network. The low number of tracer positive points during the I2 test compared to the other tracer tests could be a consequence of the actual groundwater flowpath; however, it could also reflect the disadvantages of using Rhodamine in fractured rock media (i.e., high retardation coefficient and high sorption coefficient, Leibundgut et al. 2011).

The Romanche River (S8) is positive for two tracer tests (I1 and I3-A), meaning that the EDF gallery collects only a part of the slope groundwater, the remaining reaching the river through the alluvium aquifer. Among the three tracer tests (I2, I1, I3-A), a rather homogeneous velocity (0.07–0.14 km/day) is observed for S16 and S13. These slow flows, compared to the one observed during the I4 test, demonstrate flow through micro-fissured matrix drained toward the east by N20 faults. Globally, the groundwater flows are fast and poorly hierarchized (tracers appear by intermittent pulses, without any characteristic restitution curve).

Analysis of seasonal variations and of spring mean recharge-area elevation

The isotopic abundance ratio of a water sample is expressed as $\delta^{18}O$ in ‰ with respect to the Vienna Standard Mean Ocean Water (V-SMOW). The isotopic elevation gradients show significant seasonal variation (−0.12 ‰/100 m for November–December, −0.25 ‰/100 m for January–March, −0.21 ‰/100 m for April–June and −0.18 ‰/100 m for July–September, Fig. 4). These values confirm the effect of season on the isotope fractionation and are in accordance with commonly observed values, from −0.1 to −0.36 ‰/100 m (Leibundgut et al. 2011). Some springs show either unrealistic values of elevation of the recharge area or lack of data. The $\delta^{18}O$ measured in S18 water sampled during the low-flow period indicates an elevation of the recharge area higher than the highest peak of the massif (Peak Oeilly). This inconsistency can be explained by a spring recharged by water depleted in ^{18}O. This depletion may be related to former water infiltrated during cold months (Martelloni et al. 2012; Cervi et al. 2015). The $\delta^{18}O$ measured in G1 water sampled during the low-flow period indicates an elevation of the recharge area lower than the spring itself. This inconsistency can be explained by ^{18}O enrichment due to an extended air–water contact (evaporation). Lastly, $\delta^{18}O$ data are lacking for some springs (dry springs: S9, S5, S11, S24; no sampling at S12 and S13).

The elevations of the recharge areas of the S5 and S4 springs are similar and are about 1,800 m above the highest local massif peak elevation (Peak Oeilly, 1,500 m) and below the Romanche River (Fig. 5a), but show a distinct seasonal variability (SD of 32 m for S5 and 315 m

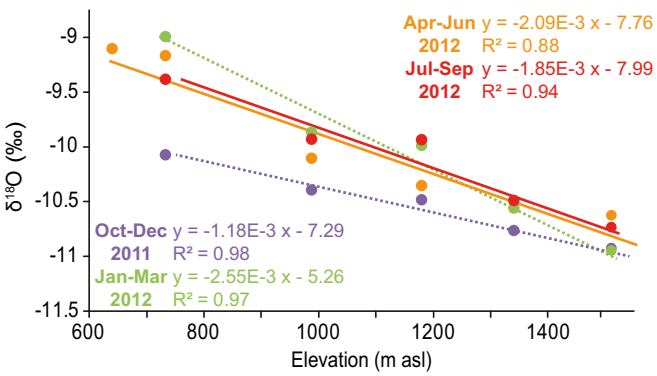

Fig. 4 Isotope elevation gradients for the four seasonal water sampling campaigns. *Solid lines* stand for precipitation isotope gradient and *dashed lines* stand for infiltration isotope gradients

DOI 10.1007/s10040-015-1298-2

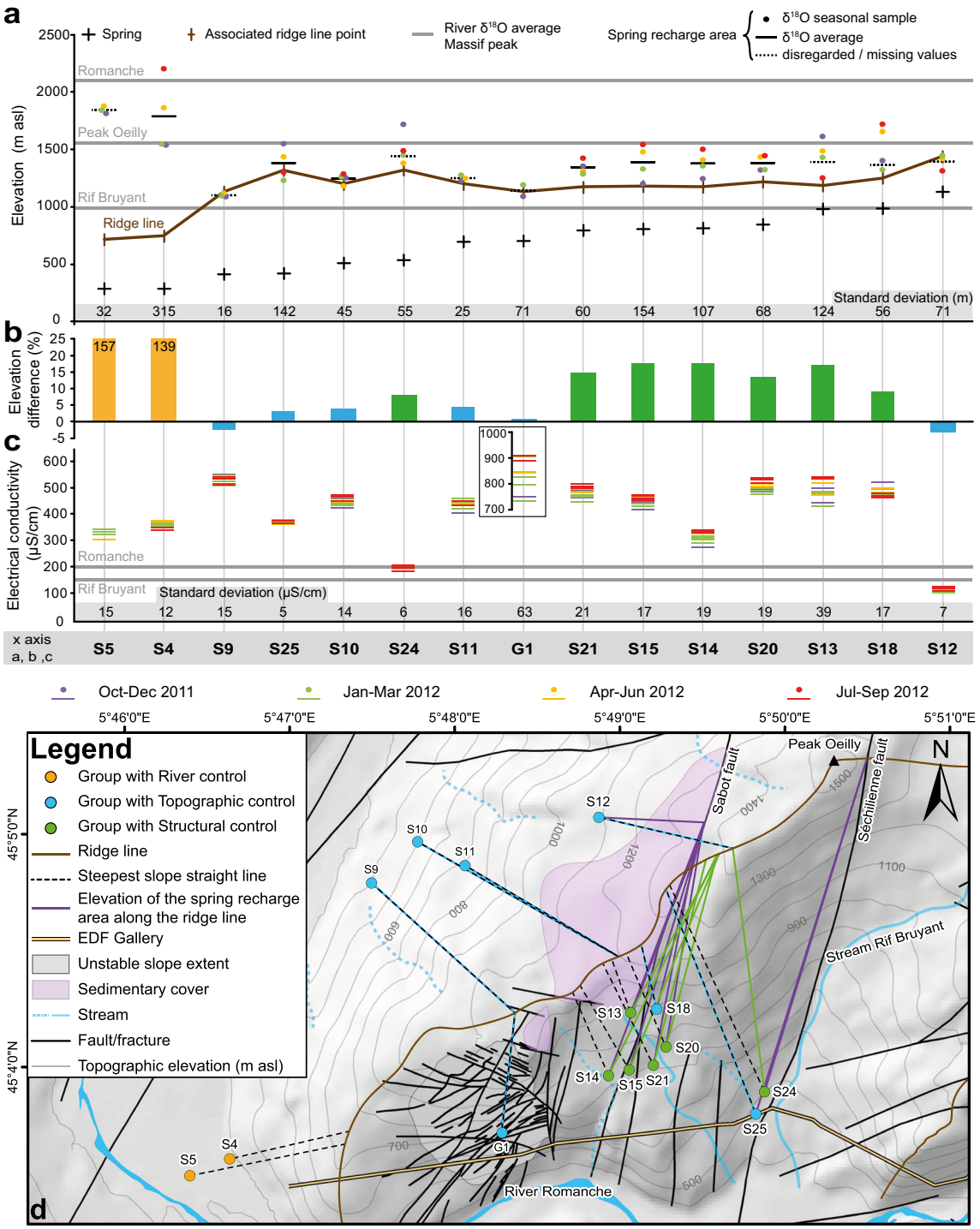

Fig. 5 Seasonal analysis of $\delta^{18}O$ and electrical conductivity of springs. **a** Seasonal $\delta^{18}O$ estimated elevation of springs plotted relative to spring elevation, associated ridgeline elevation, and $\delta^{18}O$ estimated elevation of surface network (*Romanche* and *Rif Bruyant*). **b** Difference between the average spring recharge-area elevation and the associated ridgeline point elevation. **c** Seasonal analysis of electrical conductivity plotted relative to surface network signal (Romanche and Rif Bruyant). **d** Spatial representation (map) of the $\delta^{18}O$ elevation of the spring recharge area

for S4). In addition, these springs show low values and a low variability of EC (340 µS/cm with SD of 14 µS/cm, Fig. 5c). These two springs seem to be influenced by both the massif slope groundwater and the Romanche water. The Romanche water smoothes the amplitude and the variations of the EC and increases the elevation of the recharge area and its seasonal variability (high sensitivity of drainage surface network from seasonal variations). S4 cannot be recharged by the Romanche alluvium aquifer, thus indicating that the open EDF gallery, which

DOI 10.1007/s10040-015-1298-2

withdraws water from the Romanche River, recharges the slope aquifer in its western part. S25 and S24 springs show a behaviour similar to that of S4 with low values and a low variability of EC (370 and 200 μS/cm with SD of 5 μS/cm). The hydrodynamic behaviours at seasonal time-steps of S25 and S24 are probably due to the recharge of the slope aquifer by the Rif Bruyant stream. The dilution by Rif Bruyant stream (recharge-area elevation of 1,010 m asl) certainly caused an underestimation of the recharge-area elevation of these springs. The elevation of the recharge area is thus assumed to be near the Peak Oeilly from where groundwater is drained by the main Séchilienne fault (Fig. 5d)

S21, S15, S14, S20, and S13 springs show mean elevations higher than the elevation of their associated ridgeline points (16 % higher on average, Fig. 5b). These springs further show high seasonal variabilities (SD of 100 m and 22 μS/cm on average) with the lowest EC values and recharge-area elevations observed during the high-flow period and the reverse for the low-flow periods (Fig. 5a,c). These springs are interpreted to be supplied by rapid water flow through fractures during high-flow periods (dilution) and drainage through the micro-fissured matrix during low-flow periods, mobilizing remote recharge areas. In contrast, S9, S10, and S11 springs show mean recharge-area elevation close to their associated ridgeline points (at most 4 % higher) with low seasonal variations. These springs show moderate EC variabilities (SD: 15 μS/cm) with no clear seasonal patterns. These results show that their recharge areas are mainly local and have little sensitivity to the seasonal variations (Fig. 5a,b,c), meaning that the spring flow is controlled by the micro-fissured matrix component. S18 spring is interpreted as showing an intermediate hydrodynamic behaviour at seasonal time-steps between the two previous groups.

Spring G1 was only sampled twice and it is not possible to assess clearly its seasonal variation. However, the recharge area seems mainly local as the two high-flow period surveys show a mean recharge area (1,143 m asl) close to the elevation of the associated ridgeline point. G1 shows the highest EC values (840 μS/cm) and the highest EC seasonal variability (SD: 63 μS/cm). These results are interpreted as generated by water–rock interactions between groundwater and the unstable slope rocks (Binet et al. 2009). Spring S12 has a very low conductivity (155 μS/cm), probably due to low water–rock interaction time. It also shows a scattered $\delta^{18}O$ signal. One possible explanation is that this spring is recharged by rapid water flow through the sedimentary cover.

Low-flow periods: hydrochemistry survey

The chemical composition of the monitored springs is detailed in Table 5. The Durov and Stiff diagrams (Fig. 6a,b) highlight four distinct water chemical groups reflecting groundwater flow through various geological units. Group 1 corresponds to Ca–HCO_3-rich waters (S12) with low EC values (about 100 μS/cm). Group 2

Table 5 Physico–chemical parameters and major ions of the monitoring springs in low-flow periods, from early June to late September (2010–2012)

Group	Station ID	Water Type	SN	Temp. (field)	pH (field)	EC (field)	Ca meq/L	Mg meq/L	Na meq/L	K meq/L	Cl meq/L	HCO_3 meq/L	SO_4 meq/L	SiO_2 meq/L
1	S12	Ca–HCO_3	5	10.22	7.72	120.0	0.88	0.21	0.09	0.01	0.03	0.86	0.16	0.14
2	S24	Mg–Ca– HCO_3	5	10.30	7.57	202.8	1.05	0.93	0.15	0.01	0.06	1.59	0.41	0.17
	S9	Mg–Ca– HCO_3	4	12.10	7.52	538.8	2.69	3.16	0.19	0.02	0.06	4.28	1.62	0.16
	S10	Mg–Ca– HCO_3	4	11.47	7.94	455.8	2.59	2.32	0.16	0.02	0.04	3.84	1.12	0.16
	S11	Mg–Ca-– HCO_3	2	9.90	7.75	440.5	2.50	2.32	0.14	0.02	0.04	3.75	1.06	0.15
	S25	Mg–Ca– HCO_3	5	13.66	7.86	367.0	1.95	1.87	0.18	0.02	0.08	3.04	0.75	0.16
3	G1	Mg–Ca–SO_4– HCO_3	4	11.75	8.08	872.5	5.10	4.79	0.26	0.04	0.05	3.43	5.88	0.12
	G2	Mg–Ca–SO_4	4	12.10	7.67	384.3	1.98	1.80	0.21	0.05	0.05	0.61	3.18	0.23
	G3	Mg–Ca– HCO_3–SO_4	1	10.10	7.05	314.0	1.55	2.09	NA	NA	0.33	2.64	1.03	n.a
	G4	Mg–Ca– HCO_3–SO_4	2	10.55	7.44	446.0	2.03	3.04	NA	NA	0.07	2.92	2.29	n.a
	G5	Mg–Ca–SO_4– HCO_3	3	10.10	7.37	629.7	2.22	5.07	NA	NA	0.06	3.47	3.92	0.14
4	S4	Ca–Mg–HCO_3–SO_4	5	11.22	7.56	354.8	2.88	0.68	0.21	0.02	0.18	2.05	1.36	0.12
	S13	Ca–Mg–HCO_3–SO_4	5	8.62	7.85	522.4	4.20	1.46	0.10	0.02	0.03	3.30	2.30	0.12
	S14	Ca–Mg-HCO_3–SO_4	5	11.50	7.77	332.2	2.31	1.07	0.15	0.01	0.09	2.51	0.80	0.13
	S15	Ca–Mg–HCO_3–SO_4	5	11.24	7.54	465.2	3.53	1.42	0.13	0.02	0.09	3.25	1.58	0.12
	S18	Ca–Mg–HCO_3–SO_4	5	8.92	7.63	481.8	4.06	1.21	0.10	0.01	0.13	3.87	1.36	0.12
	S20	Ca–Mg–HCO_3–SO_4	5	10.66	7.50	521.2	4.25	1.41	0.12	0.02	0.06	3.58	1.97	0.12
	S21	Ca–Mg–HCO_3–SO_4	3	12.00	7.70	499.7	3.99	1.33	0.12	0.01	0.06	3.40	1.93	0.12

DOI 10.1007/s10040-015-1298-2

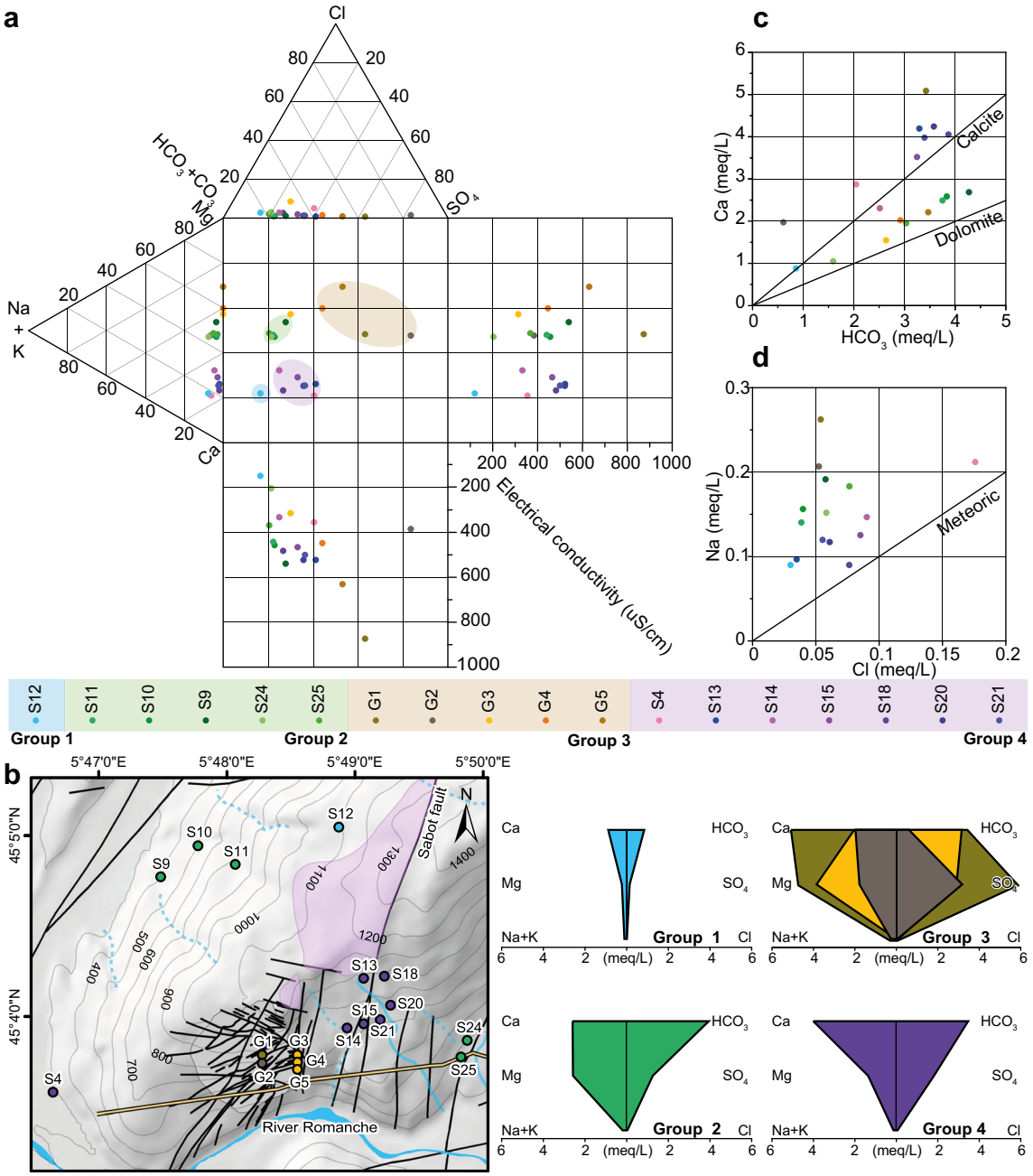

Fig. 6 Hydrochemistry analysis with **a** Durov diagram, **b** spatial representation (map) and Stiff diagrams, and scatter plots of chemical concentrations: **c** Ca vs. HCO_3 and **d** Na vs. Cl

corresponds to Mg–Ca–HCO_3-rich waters (S24, S25, S11, S10 and S9) where Ca and Mg are in the same proportions and EC is from 200 µS/cm (S24) to 540 µS/cm (S9). Water composition of group 3 has various chemical signatures and varies from Mg–Ca–HCO_3–SO_4-rich waters (G4 and G3), with intermediate Mg–Ca–SO_4–HCO_3-rich water (G5 and G1), to Mg–Ca–SO_4-rich waters (G2). The EC values vary from 300 µS/cm (G4 and G3) to 850 µS/cm (G1). Group 4 corresponds to Ca–Mg–HCO_3–SO_4-rich waters (S4, S14, S15, S18, S21, S20 and S13) with EC values varying from 350 µS/cm (S4 and S14) to 520 µS/cm (S21, S20 and S13).

Stable zone (groups 1 and 2)

The low concentrations of Ca and HCO_3 of group 1 (S12), located on the calcite equilibrium line, is representative of water circulating in a carbonate or calcite dominant cover (limestone or moraines including carbonate materials) with a short residence time (Fig. 6c). For this group, inverse modelling has been tested for the S9, S10 and S11 springs.

The results show that 91 % of the Mg concentrations come from dolomite and 9 % come from phlogopite, while 87 % of the Ca is derived from the dolomite and the remaining 13 % from the calcite. Therefore, the high Mg

DOI 10.1007/s10040-015-1298-2

concentrations are explained by water transit through the carbonate materials; however, these spring compositions are above the dolomite equilibrium line (Fig. 6c), which can be explained by the alteration of pyrite which releases protons (Eq. 1), which can then consume HCO_3 produced by dissolution of carbonate minerals (Eq. 2), thus releasing CO_2 and H_2O (Eq. 3). The δS^{34} analyses performed by Vengeon (1998) show that SO_4 has a sulfurized origin, due to alteration of pyrite. Pyrite is present only in the micaschist bedrock.

$$FeS_2 + \frac{15}{4} \times O_2 + \frac{7}{2} \times H_2O \leftrightarrow Fe(OH)_3 + 2SO_4^{2-} + 4H^+ \quad (1)$$

$$(Ca, Mg)(CO_3)_2 + 2H_2O + 2CO_2 \leftrightarrow Ca^{2+} + Mg^{2+} + 4HCO_3^- \quad (2)$$

$$HCO_3^- + H^+ \leftrightarrow H_2O + CO_2 \quad (3)$$

This succession of chemical reactions explains the range of pH (between 7 and 8) measured in the Séchilienne waters, despite the production of protons, and results in a depletion of HCO_3 ions with respect to Ca and Mg, the latter being balanced by SO_4 (Table 5). The springs of group 2 are, therefore, recharged by water which circulated through carbonates and basement formations. The low electrical conductivity values of S24 and S25 are explained by the influence of the Rif Bruyant stream, as shown by the seasonal analysis (see 'Analysis of seasonal variations and of spring mean recharge-area elevation' section).

Unstable zone (group 3)

Group 3 (G5, G4, G3, G2, G1) is characterized by the highest SO_4 concentrations (Fig. 6; Table 5), which can be explained by two mechanisms related to the slope deformation. First, the opening and/or closing of fractures lead to a new flowpath through unaltered pyrite-bearing zones (Calmels et al. 2007) and, second, the friction and grinding along fractures due to the movement of rock masses cause a refreshment of pyrite reactive surfaces, increasing the weathering rate (Binet et al. 2009). Lastly, the alteration of the pyrite promotes the alteration of carbonate and silicate (Gaillardet et al. 1999; Dongarrà et al. 2009). G1 shows high Ca and Mg concentrations (Fig. 6b,c), as well as high Na concentrations in the G710 gallery (G1 and G2, Fig. 6d). For this group, inverse modelling was tested for G1. The result shows that 58 % of the Ca concentration comes from calcite and 42 % from dolomite. Mg contents are explained by water–rock interactions mainly in the basement with a Mg origin of 37 % from dolomite and 63 % from chlorite. Water mineralization results mainly from the interaction with the basement minerals. In particular, the SO_4 content is clearly a marker of the unstable zone. The variety of the water mineralisation characteristics between the various gallery points is due to the strong mineralogical heterogeneities within the basement and within the fracture network of the unstable zone. Nevertheless, water interaction with carbonate rock is necessary to explain water chemistry content. Ca and Mg ions can originate either from the major tension cracks filled with colluvial deposits rich in limestone fragments or from water flowing from the sedimentary cover. Although the I4 tracer test indicates a supply from the sedimentary cover, the $\delta^{18}O$ analysis indicates a predominantly local recharge.

Mixing zone (group 4)

The group 4 (S4, S14, S15, S18, S21, S20 and S13) is distinguishable from other springs by its concentrations of Ca, Na and SO_4. The Ca concentrations fall near the calcite equilibrium line (Fig. 6c), reflecting a significant transit in carbonate materials. The SO_4 concentrations that are up to 25 % higher than the springs of the stable zone (group 2) can be explained by groundwater flow through the stable bedrock. A mixing test was performed with water of the carbonate sedimentary cover (S12) and water of the unstable zone (G1) to quantify the contribution of each component. The waters of group 1 are represented only by a single spring (S12), having a very small recharge area with a limited residence time, inducing a very low mineralization. This group is considered as representative of the sedimentary cover. In the modelling, group 1 mineralization has been increased 4-fold in order to account for of a longer flowpath between the sedimentary cover and group 4 (as indicated by artificial tracers, Fig. 3) and, hence, for a longer residence time. The composition of group 4 could be explained by mixing 30 % unstable-zone water and 70 % sedimentary-cover water. Lastly, S4 water is also a mixture of the Romanche River water, the stable-zone water and the unstable-zone water through drainage of the EDF gallery.

Gallery water inflows survey

Five galleries and one piezometer (P1) were surveyed (Fig. 7a). The highest gallery (G900) is always dry. The G710 gallery shows two leakages, one quasi-permanent almost dry in summer (G1), at 150 m from the entrance, and one temporary (G2) at 80 m from the entrance. Two leakage zones were also identified for the G670 gallery at 25 and 70 m from the entrance. G585 gallery shows a temporary water inflow (202 m, G3) and a permanent water inflow (160 m, G5), and a localized leakage area (170 m, G4). Water inflows of the galleries are localized near fracture-damaged zones (Vengeon 1998), reinforcing the prominent role of the fracture network in the groundwater flowpath. Although the piezometer P1 is currently clogged, the water level fluctuations were recorded between 590 and 602 m asl from November 2009 to April 2010 (Fig. 7d). P1 piezometer did not reach

DOI 10.1007/s10040-015-1298-2

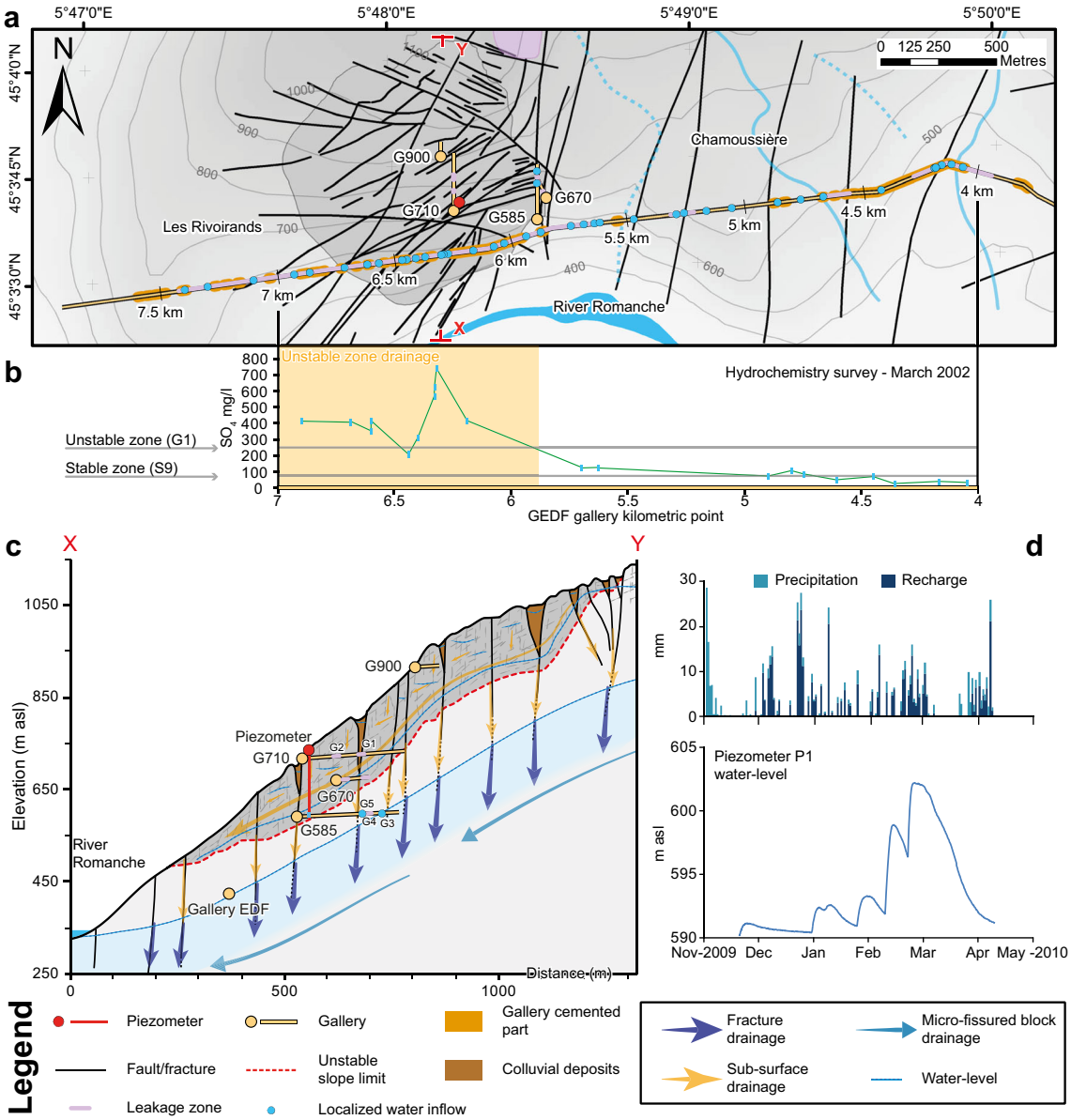

Fig. 7 Gallery survey. **a** Spatial representation (map) of water inflows. **b** SO_4 concentration of the EDF gallery water inflows. **c** Cross-section of water inflows. **d** Plot of the water level recorded in the piezometer P1 with precipitation and recharge. The cross-section of the unstable zone is modified after Lebrouc et al. (2013). The unstable slope boundary is defined according to the geophysical survey of Le Roux et al. (2011). Recharge was computed according to the computation workflow of Vallet et al. (2015)

the stable zone below the landslide body and, thus, P1 water levels are associated with rock/matrix within the landslide body. These water levels are considered as representative of high-groundwater-level conditions (Fig. 7c).

The EDF gallery, in particular, shows bare rock with limited cemented sections (revealing heavily fractured zones) with water flowing unconfined by gravity from an upstream Romanche withdrawal point. During the excavation of the EDF gallery, perennial springs located at Les Rivoirands and Chamoussière villages were permanently dried up (Fig. 7a). Numerous and scattered water inflows and leakages occur in the EDF gallery between 5.5 and 7 km, matching with the dense fracture network of the landslide (Fig. 7a). Between 3.9 and 4.5 km, the Séchilienne fault has completely damaged the zone and many water inflows occur, revealing the prominent drainage role of the fault. To a lesser extent, the Sabot fault seems to have a more localized impact on the EDF gallery water inflows. The hydrochemistry survey shows that SO_4 is the marker of the unstable slope—see section 'Unstable zone (group 3)'. From kilometric points 4 to 5.80, SO_4 content is similar to S9 and is representative of the stable zone, whereas from kilometric points 6 to 7, the SO_4 signal increases and even exceeds the concentration of G1 representative of the unstable zone (Fig. 7b). The SO_4 content confirms the prominent role of the EDF gallery in the drainage of the unstable slope.

DOI 10.1007/s10040-015-1298-2

Groundwater conceptual model

Stable zone: fractures vs. micro-fissured matrix

Two main groundwater flow types are identified: (1) rapid and reactive water flow in fractures (S4, S13, S14, S15, S20, S21, S24 and S25; seasonal analysis, Fig. 5) which bypass the bulk of the less pervious and (2) inertial water flow from micro-fissured matrix, on which springs S9, S10 and S11 depend (seasonal analysis, Fig. 5). These groundwater flows are characteristic of the dual-permeability of fractured reservoirs (Maréchal 1998; Cappa et al. 2004). Intermediate hydrodynamic behaviour between micro-fissured matrix and fractures is also observed (S18). Lastly, groundwater flow occurs in the perched aquifer located in the sedimentary cover (S12, Guglielmi et al. 2002). The main N20 Sabot fault plays a major role in the massif drainage, with a rapid transfer from the sedimentary cover, but this fault also drains the unstable zone with much lower velocities (tracer test and seasonal analysis, Figs. 3 and 5). This is confirmed by the hydrochemistry survey which showed that the springs located along the Sabot fault match with mixed water that flowed through the sedimentary cover and the unstable slope (Fig. 6, group 4); therefore, the Sabot fault has a significant spatial influence, draining out the deep aquifer below the unstable slope, likely because of a lowering of the groundwater level which, in turn, causes a west to east hydraulic gradient (tracer test, Fig. 3). Flow velocities (tracer test, Fig. 3), water mixing (hydrochemistry, Fig. 6) and the lack of fractures indicate that the unstable slope drainage is done mainly through the micro-fissured matrix and is minor in influence relative to the Sabot fault drainage axis (Fig. 8a).

The Séchilienne fault also acts as a major drainage axis and even promotes water infiltration from Rif Bruyant stream (seasonal analysis, Fig. 5). Outside of the major fault or fracture zones, the groundwater behaviour is more inertial, being characterized by a longer residence time. This is testified by the hydrodynamical behaviour of the springs of the northern slope of the Mont Sec massif. The hydrodynamic behaviour of the S18 spring is typical of a spring supplied by the micro-fissured matrix with very small influence from conductive fractures.

Unstable zone: landslide perched aquifer

During the low-flow period, the water level of the piezometer P1 dropped below 590 m asl and therefore below the boundary of the unstable zone. Unsaturated zones have been observed in all galleries (gallery survey, Fig. 7). In contrast, during almost all the high-flow periods, the water level of P1 (about 600 m asl) suggests a saturated zone at the base of the unstable zone below the G710 gallery. Moreover, during high-flow periods, a shallow continuous drainage (tracer tests, Fig. 3) occurs through the landslide, draining water from the sedimentary cover (I4 tracer test, Fig. 3a). This recharge mechanism involves a hydraulic connection of the unstable zone with the sedimentary perched aquifer which bypasses the deep aquifer (Fig. 8), which indicates that, in high-flow periods, the recharge area is much larger than the landslide surface (Guglielmi et al. 2002; Cappa et al. 2004). However, the water from the G710 gallery has mainly a local origin (seasonal analysis, Fig. 5) with a characteristic SO_4 concentration explained by mechanical weathering rather than by variations of residence time (hydrochemistry, Fig. 6), which shows that the recharge of the unstable perched aquifer is mainly local and that the contribution of the remote groundwater from the sedimentary cover is limited (Fig. 8).

Heterogeneous, anisotropic and discontinuous properties of the landslide (Binet 2006) lead to a perched discontinuous fractured reservoir slope which is better described by numerous disconnected saturated zones rather than by a single one (Cappa et al. 2004, Figs. 7c and 8b). This discontinuous reservoir is temporary since it is rapidly drained by the dense fracture network as demonstrated by intra-annual variability of the leakage flow and water chemistry content of the landslide galleries (seasonal analysis and gallery survey, Figs. 5 and 7). The recharge is essentially local, enhanced by the trenches and the counterscarps which tend to limit the runoff and to facilitate groundwater infiltration in the landslide area (Binet et al. 2007a). During high-flow periods, the waters infiltrated in the landslide flow perpendicularly to the slope through the dense network of near-vertical N70 conductive fractures down to a basal continuous perched aquifer (vertical drainage), which is maintained as saturated by the high recharge amount. When the recharge amount is sufficient, the numerous disconnected saturated zones can become temporarily connected, leading to a groundwater flow parallel to the slope down to the landslide (horizontal drainage). This near-surface drainage, above the basal perched aquifer, occurs in the unsaturated zone and is controlled by the N70 fractures nearly parallel to the slope. In contrast, during the dry season, the recharge amount is not sufficient to maintain a continuous perched aquifer in the landslide and only temporarily disconnected saturated zones can occur after storm events. The numerous disconnected saturated zones likely result from the high vertical gradient of the hydraulic conductivity (Maréchal 1998) and the heterogeneity of the landslide, particularly the tension cracks filled by colluvial deposits and altered materials (Cappa et al. 2004). An interpretative position of the perched-aquifer water level during the high-flow periods is suggested along the cross-sections XY in Fig. 7c and XYZ in Fig. 8b.

Unstable zone: slope deep aquifer

The EDF gallery acts as a main drainage structure for the slope (tracer test, Fig. 3), and especially beneath the unstable zone, where the fracture network is very dense (gallery survey, Fig. 7b). The EDF gallery imposes a constant head of the deep aquifer at about 425 m asl

 DOI 10.1007/s10040-015-1298-2

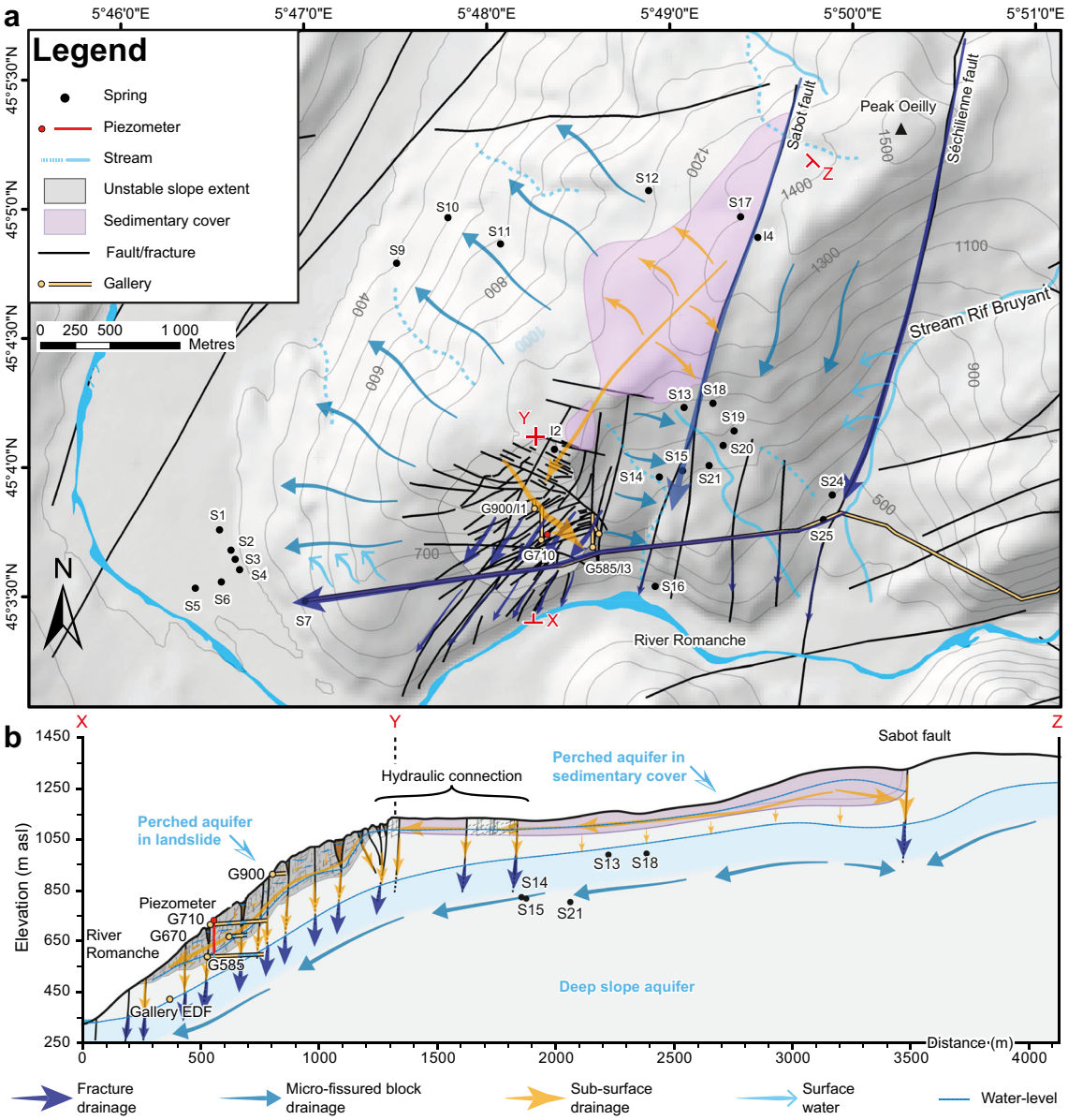

Fig. 8 Sketch of the groundwater conceptual model. **a** Spatial sketch. **b** Cross-section sketch. The cross-section of the unstable zone is modified after Lebrouc et al. (2013). The unstable slope boundary is defined according to the geophysical survey of Le Roux et al. (2011). *S14*, *S15*, *S21*, *S13* and *S18* springs are projected on the cross-section

(Fig. 7c). The deep-aquifer water level is also controlled by the constant water head of the Romanche alluvium. The EDF gallery on its western side recharges the deep aquifer with water from the Romanche River and water inflow from the unstable zone (seasonal analysis and hydrochemistry, Figs. 5 and 6). The EDF gallery acts as a major east–west drain, whose influence is mainly controlled by the N70 crossing fractures (Fig. 8a). Groundwater which is not collected by the EDF gallery flows toward the Romanche alluvium aquifer or to the springs located westward (tracer-test, Fig. 3c,d). All this information allows for the proposal of an interpretative position of the deep-aquifer water level (Figs. 7c and 8b).

Conclusion

This study highlights the dual-permeability properties of fractured-rock reservoirs with preferential water flow in fractures bypassing most of the less pervious and inertial micro-fissured matrix. The major faults or fractures play a key role in the massif drainage. The EDF gallery also acts as a major drain in the massif. This survey highlights the contrast in hydraulic properties between the unstable zone and the intact rock mass outside the landslide. This vertical heterogeneity leads to a two-layer aquifer, with a shallow perched aquifer localized in the unstable zone and a deep aquifer in the whole massif. The landslide perched aquifer is temporary and mainly discontinuous, and its extent and

DOI 10.1007/s10040-015-1298-2

connectivity fluctuate according to short-term recharge variations. The perched aquifer is almost dry during the low-flow periods. The groundwater flows mainly through a dense network of widely opened fractures. The recharge area of the landslide perched aquifer is mainly local although, in high-flow periods, the recharge area may become larger than the landslide surface and may include the remote sedimentary cover perched aquifer.

Seasonal monitoring of natural and artificial tracers enables characterization of the groundwater scheme of unstable slopes and their surrounding stable massif. The results obtained in the case of the Séchilienne landslide show that this method is able to solve various important issues for hydromechanical studies (Cappa et al. 2014). Due to the general scarcity of hydrogeological monitoring networks in landslide sites, the proposed method could be suitable to conceive outstanding flow schemes for other landslide types.

Acknowledgements This research was funded by SLAMS (Séchilienne Land movement: Multidisciplinary Studies), the program of the Agence Nationale de la Recherche. The meteorological and displacement data were supplied by CEREMA Lyon. The authors gratefully acknowledge the support of Jean-Pierre Duranthon and Marie-Aurélie Chanut (CEREMA Lyon). The authors are also very grateful to Christophe Loup (UMR Chrono-Environnement) for the chemical analyses. The implementation of the monitoring network would not have been possible without the cooperation of Mrs. and Mr. Aymoz, Patrick Boyer from the Office National des Forêts, and Gérard Cret, mayor of Séchilienne. The manuscript was improved by detailed and constructive comments from the editor Jiu Jimmy Jiao, the associate editor Jürgen Mahlknecht, and reviewers Stéphane Binet, Federico Cervi, Boris Matti and one anonymous reviewer.

References

Abellán A, Michoud C, Jaboyedoff M, et al (2015) Velocity Prediction on Time-Variant Landslides Using Moving Response Functions: Application to La Barmasse Rockslide (Valais, Switzerland). In: Lollino G, Giordan D, Crosta GB, et al. (eds) Engineering Geology for Society and Territory - vol 2. Springer International Publishing, pp 323–327

Agliardi F, Crosta G, Zanchi A (2001) Structural constraints on deep-seated slope deformation kinematics. Eng Geol 59:83–102. doi:10.1016/S0013-7952(00)00066-1

Alfonsi P (1997) Relation entre les paramètres hydrologiques et la vitesse dans les glissements de terrains. Exemples de La Clapière et de Séchilienne. Rev Fr Géotech 79:3–12

Atteia O (1994) Major and trace elements in precipitation on western Switzerland. Atmos Environ 28:3617–3624. doi:10.1016/1352-2310(94)00193-O

Barféty J-C, Bordet P, Carme J, et al. (1972) Notice et carte géologique de la France au 1/50000, feuille de Vizille numéro 797 [Explanatory note and geological map of France at 1/50000, Vizille sheet number 797]. Bureau de recherches géologiques et minières, Orléans, France

Barla G, Chiriotti E (1995) Insights into the behaviour of the large deep-seated gravitational slope deformation of Rosone, in the Piemonte Region (Italy). Proc. 44th Geomech. Colloquim. Austrian Soc. for Geomechanics, Salzburg, Austria, pp 425–432

Belle P, Aunay B, Bernardie S et al (2014) The application of an innovative inverse model for understanding and predicting landslide movements (Salazie cirque landslides, Reunion Island). Landslides 11:343–355. doi:10.1007/s10346-013-0393-5

Bernardie S, Desramaut N, Malet J-P et al (2014) Prediction of changes in landslide rates induced by rainfall. Landslides 12(3):1–14. doi: 10.1007/s10346-014-0495-8

Binet S (2006) L'hydrochimie, marqueur de l'évolution à long terme des versants montagneux fracturés vers de grands mouvements de terrain: application à plusieurs échelles sur la haute vallée de la Tinée (Mercantour, France) et sur le versant de Rosone (Gran Paradiso, Italie) [Hydrochemistry, a marker of long-term evolution of unstable fractured slopes, towards large moving rock masses: application at multiple scales on the upper valley of the Tinée (Mercantour, France) and on the slope of (Gran Paradiso, Italy]. PhD Thesis, Université de Franche-Comté, France

Binet S, Guglielmi Y, Bertrand C, Mudry J (2007a) Unstable rock slope hydrogeology: insights from the large-scale study of western Argentera-Mercantour hillslopes (south-east France). Bull Soc Géol Fr 178:159–168. doi:10.2113/gssgfbull.178.2.159

Binet S, Jomard H, Lebourg T et al (2007b) Experimental analysis of groundwater flow through a landslide slip surface using natural and artificial water chemical tracers. Hydrol Process 21:3463–3472. doi:10.1002/hyp.6579

Binet S, Spadini L, Bertrand C et al (2009) Variability of the groundwater sulfate concentration in fractured rock slopes: a tool to identify active unstable areas. Hydrol Earth Syst Sci 13:2315–2327. doi:10.5194/hess-13-2315-2009

Bogaard T, Guglielmi Y, Marc V et al (2007) Hydrogeochemistry in landslide research: a review. Bull Soc Géol Fr 178:113–126. doi:10.2113/gssgfbull.178.2.113

Bonnard C (1988) Landslides/Glissements De Terrain: Proceedings of the 5th International Symposium, Lausanne, 10–15 July 1988, 1st edn. Taylor and Francis, Rotterdam, The Netherlands

Bonzanigo L, Eberhardt E, Loew S (2007) Long-term investigation of a deep-seated creeping landslide in crystalline rock, part I: geological and hydromechanical factors controlling the Campo Vallemaggia landslide. Can Geotech J 44:1157–1180. doi:10.1139/T07-043

Calmels D, Gaillardet J, Brenot A, France-Lanord C (2007) Sustained sulfide oxidation by physical erosion processes in the Mackenzie River basin: climatic perspectives. Geology 35:1003–1006. doi:10.1130/G24132A.1

Cappa F, Guglielmi Y, Soukatchoff VM et al (2004) Hydromechanical modeling of a large moving rock slope inferred from slope levelling coupled to spring long-term hydrochemical monitoring: example of the La Clapière landslide (Southern Alps, France). J Hydrol 291:67–90. doi:10.1016/j.jhydrol.2003.12.013

Cappa F, Guglielmi Y, Rutqvist J et al (2006) Hydromechanical modelling of pulse tests that measure fluid pressure and fracture normal displacement at the Coaraze Laboratory site, France. Int J Rock Mech Min Sci 43:1062–1082. doi:10.1016/j.ijrmms.2006.03.006

Cappa F, Guglielmi Y, Viseur S, Garambois S (2014) Deep fluids can facilitate rupture of slow-moving giant landslides as a result of stress transfer and frictional weakening. Geophys Res Lett 41:61–66. doi:10.1002/2013GL058566

Cervi F, Corsini A, Doveri M, et al (2015) Characterizing the Recharge of Fractured Aquifers: A Case Study in a Flysch Rock Mass of the Northern Apennines (Italy). In: Lollino G, Arattano M, Rinaldi M, et al. (eds) Engineering Geology for Society and Territory - vol 3. Springer International Publishing, pp 563–567

Cervi F, Ronchetti F, Martinelli G et al (2012) Origin and assessment of deep groundwater inflow in the Ca' Lita landslide using hydrochemistry and in situ monitoring. Hydrol Earth Syst Sci 16:4205–4221. doi:10.5194/hess-16-4205-2012

Chanut M-A, Vallet A, Dubois L, Duranthon J-P (2013) Mouvement de versant de Séchilienne: relations entre déplacements de surface et précipitations—analyse statistique [Séchilienne landslide: relationships between surface displacements and precipitations—statistical analysis]. Journées Aléa Gravitaire, Grenoble, September 2013

Charlier J-B, Bertrand C, Binet S et al (2010) Use of continuous measurements of dissolved organic matter fluorescence in groundwater to characterize fast infiltration through an unstable fractured hillslope (Valabres rockfall, French Alps). Hydrogeol J 18:1963–1969. doi:10.1007/s10040-010-0670-5

Clark ID, Fritz P (1997) Environmental isotopes in hydrogeology. CRC, Boca Raton, LA

Clauser C (1992) Permeability of crystalline rocks. EOS Trans Am Geophys Union 73:233–238. doi:10.1029/91EO00190

Corominas J, Moya J, Ledesma A et al (2005) Prediction of ground displacements and velocities from groundwater level changes at the Vallcebre landslide (Eastern Pyrenees, Spain). Landslides 2:83–96. doi:10.1007/s10346-005-0049-1

Dongarrà G, Manno E, Sabatino G, Varrica D (2009) Geochemical characteristics of waters in mineralised area of Peloritani Mountains (Sicily, Italy). Appl Geochem 24:900–914. doi:10.1016/j.apgeochem.2009.02.002

Durville J-L, Kasperki J, Duranthon J-P (2009) The Séchilienne landslide: monitoring and kinematics. First Ital. Workshop on Landslides, Naples, Italy, June 2009, pp 174–180

Gaillardet J, Dupré B, Louvat P, Allègre CJ (1999) Global silicate weathering and CO_2 consumption rates deduced from the chemistry of large rivers. Chem Geol 159:3–30. doi:10.1016/S0009-2541(99)00031-5

Gat JR (1996) Oxygen and hydrogen isotopes in the hydrologic cycle. Annu Rev Earth Planet Sci 24:225–262. doi:10.1146/annurev.earth.24.1.225

Guglielmi Y, Vengeon JM, Bertrand C et al (2002) Hydrogeochemistry: an investigation tool to evaluate infiltration into large moving rock masses (case study of La Clapière and Séchilienne alpine landslides). Bull Eng Geol Environ 61:311–324

Guglielmi Y, Cappa F, Binet S (2005) Coupling between hydrogeology and deformation of mountainous rock slopes: insights from La Clapière area (southern Alps, France). C R Geosci 337:1154–1163. doi:10.1016/j.crte.2005.04.016

Helmstetter A, Garambois S (2010) Seismic monitoring of Séchilienne rockslide (French Alps): analysis of seismic signals and their correlation with rainfalls. J Geophys Res 115, F03016. doi:10.1029/2009JF001532

Hilley GE, Chamberlain CP, Moon S et al (2010) Competition between erosion and reaction kinetics in controlling silicate-weathering rates. Earth Planet Sci Lett 293:191–199. doi:10.1016/j.epsl.2010.01.008

Hong Y, Hiura H, Shino K et al (2005) The influence of intense rainfall on the activity of large-scale crystalline schist landslides in Shikoku Island, Japan. Landslides 2:97–105. doi:10.1007/s10346-004-0043-z

Iverson RM (2000) Landslide triggering by rain infiltration. Water Resour Res 36:1897–1910. doi:10.1029/2000WR900090

Kosugi K, Fujimoto M, Katsura S et al (2011) Localized bedrock aquifer distribution explains discharge from a headwater catchment. Water Resour Res 47, W07530. doi:10.1029/2010WR009884

Le Roux O, Jongmans D, Kasperski J et al (2011) Deep geophysical investigation of the large Séchilienne landslide (western Alps, France) and calibration with geological data. Eng Geol 120:18–31. doi:10.1016/j.enggeo.2011.03.004

Lebrouc V, Schwartz S, Baillet L et al (2013) Modeling permafrost extension in a rock slope since the Last Glacial Maximum: application to the large Séchilienne landslide (French Alps). Geomorphology 198:189–200. doi:10.1016/j.geomorph.2013.06.001

Leibundgut C, Maloszewski P, Külls C (2011) Tracers in hydrology. Wiley, New York

Lin P-Y, Tsai LL-Y (2012) A hydrochemical study of Hungtsaiping landslide area, Nantou, Taiwan. Environ Earth Sci 67:1045–1060. doi:10.1007/s12665-012-1564-8

Lis G, Wassenaar LI, Hendry MJ (2008) High-precision laser spectroscopy D/H and $^{18}O/^{16}O$ measurements of microliter natural water samples. Anal Chem 80:287–293. doi:10.1021/ac701716q

Maréchal J-C (1998) Les circulations d'eau dans les massifs cristallins alpins et leurs relations avec les ouvrages souterrains [Groundwater flows in Alpine crystalline massifs and their relationships with man-made excavation]. PhD Thesis, Ecole Polytechnique Fédérale de Lausanne (EPFL), Switzerland

Maréchal J-C, Etcheverry D (2003) The use of ^{3}H and $\delta^{18}O$ tracers to characterize water inflows in Alpine tunnels. Appl Geochem 18:339–351

Martelloni G, Segoni S, Fanti R, Catani F (2012) Rainfall thresholds for the forecasting of landslide occurrence at regional scale. Landslides 9:485–495. doi:10.1007/s10346-011-0308-2

Meric O, Garambois S, Jongmans D et al (2005) Application of geophysical methods for the investigation of the large gravitational mass movement of Séchilienne, France. Can Geotech J 42:1105–1115. doi:10.1139/t05-034

Michoud C, Bazin S, Blikra LH et al (2013) Experiences from site-specific landslide early warning systems. Nat Hazards Earth Syst Sci 13:2659–2673. doi:10.5194/nhess-13-2659-2013

Padilla C, Onda Y, Iida T et al (2014) Characterization of the groundwater response to rainfall on a hillslope with fractured bedrock by creep deformation and its implication for the generation of deep-seated landslides on Mt. Wanitsuka, Kyushu Island. Geomorphology 204:444–458. doi:10.1016/j.geomorph.2013.08.024

Parkhurst DL, Appelo CAJ (1999) User's guide to PHREEQC (version 2): a computer program for speciation, batch-reaction, one-dimensional transport, and inverse geochemical calculations. Water-Resources Investigations Report 99-4259

Penna D, Stenni B, Šanda M et al (2010) On the reproducibility and repeatability of laser absorption spectroscopy measurements for $\delta^{2}H$ and $\delta^{18}O$ isotopic analysis. Hydrol Earth Syst Sci 14:1551–1566. doi:10.5194/hess-14-1551-2010

Pili É, Perrier F, Richon P (2004) Dual porosity mechanism for transient groundwater and gas anomalies induced by external forcing. Earth Planet Sci Lett 227:473–480. doi:10.1016/j.epsl.2004.07.043

Rochet L, Giraud A, Antoine P, Évrard H (1994) La déformation du versant sud du Mont-Sec dans le secteur des Ruines de Séchilienne (Isère) [The deformation of the Mont Sec slope in the Ruines de Séchilienne area (Isère)]. Bull Int Assoc Eng Geol 50:75–87. doi:10.1007/BF02594959

Ronchetti F, Borgatti L, Cervi F et al (2009) Groundwater processes in a complex landslide, northern Apennines, Italy. Nat Hazards Earth Syst Sci 9:895–904. doi:10.5194/nhess-9-895-2009

Rutqvist J, Stephansson O (2003) The role of hydromechanical coupling in fractured rock engineering. Hydrogeol J 11:7–40. doi:10.1007/s10040-002-0241-5

Sun J, Liu Q, Li J, An Y (2009) Effects of rainfall infiltration on deep slope failure. Sci China Ser G Phys Mech Astron 52:108–114. doi:10.1007/s11433-009-0004-6

Tullen P (2002) Méthodes d'analyse du fonctionnement hydrogéologique des versants instables [Methods of analyses of the hydrogeological functioning of unstable slopes]. PhD Thesis, Ecole Polytechnique Fédérale de Lausanne, Switzerland

Vallet A, Bertrand C, Fabbri O, Mudry J (2015) An efficient workflow to accurately compute groundwater recharge for the study of rainfall-triggered deep-seated landslides, application to the Séchilienne unstable slope (western Alps). Hydrol Earth Syst Sci 19:427–449. doi:10.5194/hess-19-427-2015

Van Asch TWJ, Buma J, van Beek LP (1999) A view on some hydrological triggering systems in landslides. Geomorphology 30:25–32. doi:10.1016/S0169-555X(99)00042-2

Vengeon JM (1998) Déformation et rupture des versants en terrain métamorphique anisotrope: apport de l'étude des Ruines de Séchilienne [Deformation and rupture of slopes in anisotropic metamorphic rocks: contribution of the study of the Ruines de Séchilienne]. PhD Thesis, Université Joseph Fourier, France